

# Two-colour high-purity Einstein-Podolsky-Rosen photonic state

Tulio Brito Brasil,<sup>1,\*</sup> Valeriy Novikov,<sup>1,\*</sup> Hugo Kerdoncuff,<sup>2</sup> Mikael Lassen,<sup>2</sup> and Eugene Polzik<sup>1</sup>

<sup>1</sup>*Niels Bohr Institute, University of Copenhagen, Copenhagen, Denmark*

<sup>2</sup>*Danish Fundamental Metrology, Hørsholm, Denmark.*

Entanglement is the backbone of quantum information science and its applications [1]. Entangled states of light are necessary for distributed quantum protocols, quantum sensing [2] and quantum internet [3]. A distributed quantum network requires entanglement between light modes of different colour optimized for interaction with the nodes as well as for communication between them. Here we demonstrate high-purity Einstein-Podolsky-Rosen (EPR) entangled state between light modes with the wavelengths separated by more than 200 nm. The modes display  $-7.7 \pm 0.5$  dB of two-mode entanglement and an overall state purity of  $0.63 \pm 0.16$ . Entanglement is observed over five octaves of sideband frequencies from rf down to audio-band. In the context of two-colour entanglement, the demonstrated combination of high state purity, strong entanglement, and extended frequency range paves the way to new matter-light quantum protocols, such as teleportation between disparate quantum systems [4], quantum sensing [2, 5, 6] and quantum-enhanced gravitational wave interferometry [7, 8]. The scheme demonstrated here can be readily applied towards entanglement between telecom wavelengths and atomic quantum memories [9, 10].

The nonlinear optics toolbox is the primary resource for generating photonic entangled states in continuous variables (CV). The  $\chi^{(2)}$  nonlinearity is usually explored to produce single-mode squeezed states, where the noise in one quadrature is suppressed beyond the vacuum field fluctuations. The interference of single-mode squeezed states have been used to demonstrate strong two-mode entanglement [11, 12], but this method limits the EPR states to be monochromatic.

As alternatives, second-harmonic generation (SHG) [13] and the process of non-degenerate parametric down-conversion [14, 15] allow for the generation of correlations between modes at different frequencies. The non-degenerate parametric process produces nonclassical correlation via annihilation of a photon with the frequency  $\omega_0$  (pump) generating twin photons pairs with frequencies  $\omega_1$  (signal) and  $\omega_2$  (idler); satisfying  $\omega_0 = \omega_1 + \omega_2$  and having the squeezed state production as the case where  $\omega_1 = \omega_2$ .

Previous approaches to generation of multi-colour quantum correlations with frequency non-degenerate optical parametric oscillators (NOPO) differ significantly

from the degenerate case due to the lack of frequency-matched local oscillators (LOs). Operation above the oscillation threshold has been used to overcome this problem, but it increases the complexity of the system making it more susceptible to noise contamination and resulting in modest levels of entanglement [16–18]. Noteworthy, to the best of our knowledge, low-frequency ( $< 500$  kHz) two-colour entanglement relevant for sensing applications has never been demonstrated.

Here we demonstrate a high-quality, tunable and versatile two-colour entanglement source enabled by a novel experimental scheme. Two coherent laser sources are upconverted via the sum-frequency generation (SFG)  $\omega_1 + \omega_2 = \omega_{\text{SFG}}$ , and the output is used as a pump beam for the NOPO below threshold, see Figure 1. The entangled output modes of the NOPO,  $\Omega_{1,i}$  and  $\Omega_{2,i}$  centered around two different colours of the lasers,  $\omega_1$ ,  $\omega_2$ , respectively, are separated and superimposed with the coherent states at  $\omega_1$  and  $\omega_2$  enabling independent detection and entanglement verification. Optoelectronic control of the double-resonance NOPO and wide tunability of the relative phases of the four quadrature operators allow for generation of robust and strong two-colour EPR entanglement. The particular choice of the wavelengths of the entangled modes at 852 nm and 1064 nm has been motivated by the envisioned application for entanglement-enhanced gravitational wave interferometry [7, 8].

To demonstrate the quantum correlations, we apply the EPR-paradox framework [19, 20] of Reid’s EPR criterion [21]. In this context, we reproduce the original EPR-paradox situation if by measurements on one the subsystems one can infer the expected values of variables in the other subsystem in such a way as to obtain an apparent violation of the Heisenberg uncertainty principle. Consider noncommuting variables associated with the signal (1) and idler (2) field quadratures,  $[x_j, y_j] = 2i$ ,  $j \in \{1, 2\}$ . We take the violation of the inequality defined in [21, 22] as the measure of the EPR entanglement as follows

$$\mathcal{E} = \Delta_{1|2}(x_1; x_2) \Delta_{1|2}(y_1; y_2) < 1, \quad (1)$$

where the conditional uncertainty is defined as  $\Delta_{1|2}(O_1; O_2) = \min_w \Delta(O_1 - w O_2)$ , with the parameter  $w_O \in \mathbb{R}$ . This was later recognized as an EPR-steering criterion and is sufficient and necessary for Gaussian states [22], ruling out the local state description of the system (1) or (2). Moreover,  $\mathcal{E}^2$  can be used as a quantifier for the degree of EPR entanglement in a system [20].

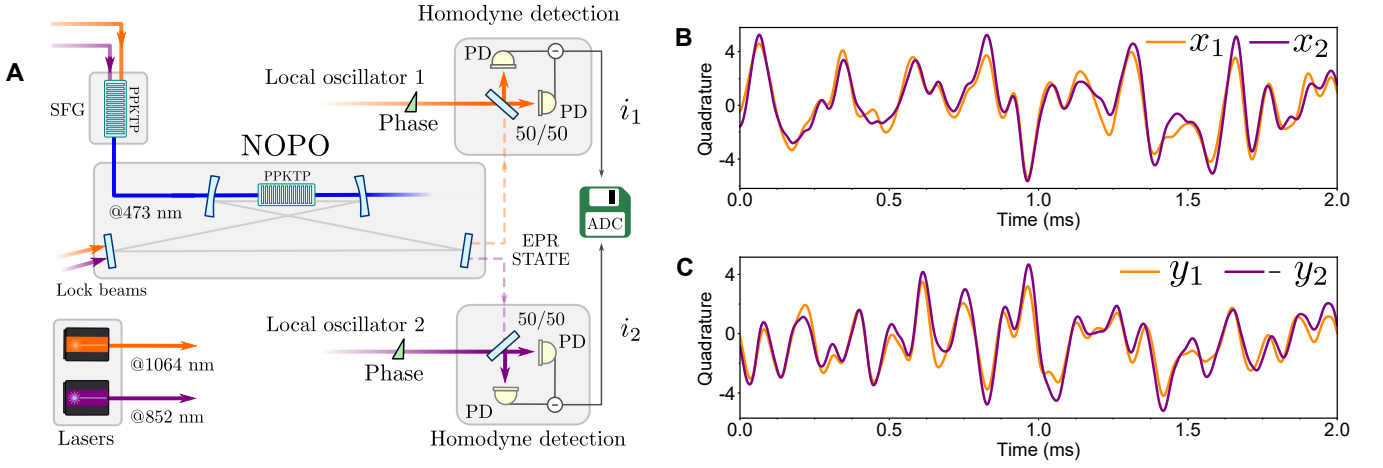


Figure 1. (A) Scheme of the experimental setup. The 852 nm and 1064 nm lasers produce the local oscillators and the blue light used to pump the NOPO through the sum-frequency generation. The entangled modes at the two colours emerging from the NOPO are separated with a dichroic mirror, mixed with the LOs, and measured by the homodyne detectors. The photocurrents are recorded by the analog-to-digital converter (ADC) to obtain information on the joint system operators. (B-C) The experimental realizations of the photocurrents  $i_1$  and  $i_2$  showing strong non-classical correlations for  $\{x_1, x_2\}$  and  $\{y_1, -y_2\}$ . Here the signals were demodulated at 200 kHz and integrated by a 10 kHz low-pass filter. The quadrature values are in vacuum state units.

Another necessary and sufficient entanglement criterion for Gaussian states is based on the inequality [23, 24]

$$V^{\text{EPR}} = \text{Var} \left[ \frac{x_1 - x_2}{\sqrt{2}} \right] + \text{Var} \left[ \frac{y_1 + y_2}{\sqrt{2}} \right] < 2, \quad (2)$$

where the sum of variances  $V^{\text{EPR}}$  allows finding the entanglement of formation (EoF) [25] which defines a number of e-bits that can be distilled from the state.

The theory comprising the dynamics of the EPR variables from a NOPO can be found in [15, 26]. In a nutshell, the generalized quadrature operator  $x_1(\theta) \equiv e^{i\theta} a_1^\dagger + e^{-i\theta} a_1$  is correlated with  $x_2(-\theta)$ , while  $y_1(\theta) \equiv x_1(\theta + \pi/2)$  is anticorrelated with  $y_2(-\theta)$ , here the pump phase is taken as a reference. The variances of the two-mode operators  $X^\pm(\theta) = [x_1(\theta) \pm x_2(-\theta)]/\sqrt{2}$ ,  $Y^\pm(\theta) \equiv X^\pm(\theta + \pi/2)$  in case of symmetric losses are given by the well-known expressions [26]

$$V_{X^\pm} = 1 \pm \eta^{\text{tot}} \frac{4\sqrt{\sigma}}{\tilde{\Omega}^2 + (1 \mp \sqrt{\sigma})^2}, \quad (3)$$

$$V_{Y^\pm} = 1 \mp \eta^{\text{tot}} \frac{4\sqrt{\sigma}}{\tilde{\Omega}^2 + (1 \pm \sqrt{\sigma})^2}, \quad (4)$$

where  $\sigma = P/P_{\text{th}}$  is the pump power ( $P$ ) normalized by the threshold power ( $P_{\text{th}}$ ),  $\tilde{\Omega} = \Omega/\delta\nu$  is the measured noise sideband frequency ( $\Omega$ ) normalized by the cavity bandwidth ( $\delta\nu$ ), and  $\eta^{\text{tot}}$  is the total efficiency [15, 26]. Thus the sum and the difference of the quadratures behave as two independent single-mode squeezed subspaces.

Several factors may affect the observation of optimum entanglement. Squeezing in  $X^-$  and  $Y^+$  is the signature of EPR correlations, but asymmetric losses may require

optimization of the quadrature combination to achieve the best value of cross-correlations [15]. Another limitation is due to the angular jitter of the noise ellipse, leading to a projection of anti-squeezing onto the squeezed quadrature [27]. The effect of the phase noise of an arbitrary quadrature operator  $Q(\theta)$  can be modeled by

$$V_Q(\delta\theta_n) = \cos^2(\delta\theta_n)V_{Q(\theta)} + \sin^2(\delta\theta_n)V_{Q(\theta+\pi/2)}, \quad (5)$$

where  $\delta\theta_n$  is the RMS phase noise. Therefore, for a finite  $\delta\theta_n$  the highest level of noise reduction is achieved at a specific pump power. Because phase noise is always present, below we use  $V_Q$  and  $V_{Q(\delta\theta_n)}$  interchangeably.

The layout of the experimental setup is presented in Fig. 1a. We measure the field quadratures from the NOPO output to observe correlations and determine the EPR entanglement between the signal and idler beams. Each of the two entangled modes is directed to a balanced homodyne detector to be mixed with the corresponding local oscillator — control of the relative phase between the local oscillator and the entangled mode selects which quadrature is projected into the photocurrents  $i_1 \propto x_1(\theta_1)$  and  $i_2 \propto x_2(\theta_2)$ . Figs. 1 (b-c) show the experimental realizations of the photocurrents presenting strong non-classical correlations between the quadrature measurements by the two detectors.

The relative phase  $\theta_j = \phi_j^{\text{OPO}} - \phi_j^{\text{LO}}$  is recovered from the interference between the local oscillator and a weak back reflection of the cavity lock beam (Fig. 1a) from the intracavity nonlinear crystal. We use this interference information to control the phase in each LO path with a PZT and to select which quadrature to measure (see Supplementary Information). The observables  $X^\pm$  ( $Y^\pm$ )

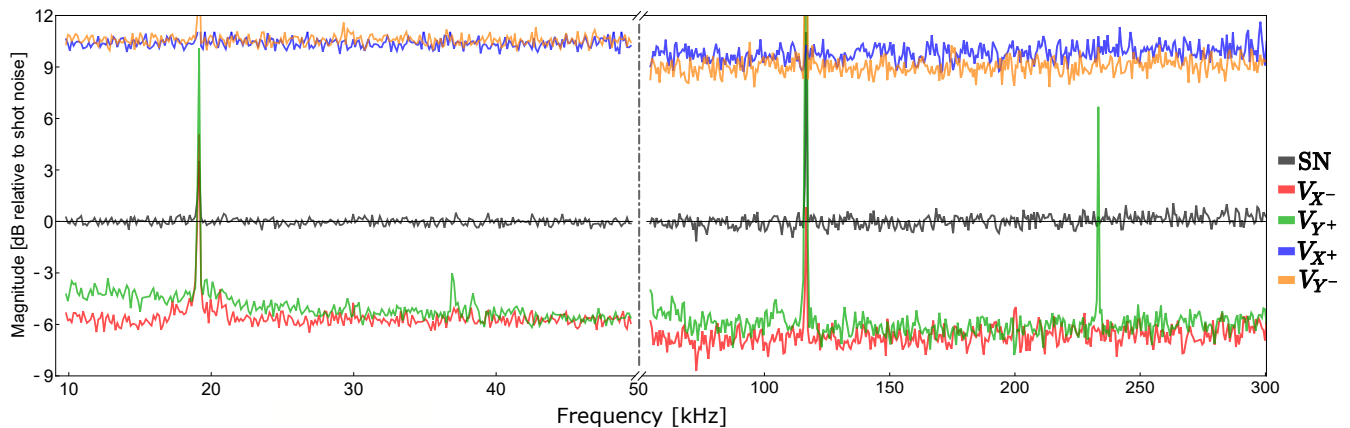


Figure 2. Spectra of the EPR quadratures normalized to shot-noise level (SN) for the frequency range 10 to 300 kHz. The left traces show the quantum noise suppression optimized for low spectral frequencies (10-50 kHz), while the right part corresponds to the best entanglement level achieved in 50-300 kHz spectral range (see text below). The narrow peaks come from the phase noise of the lasers. The data are corrected for electronic noise which is 18.5 dB below the shot-noise level.

are recorded by initially setting of  $\theta_1 = \theta_2 = 0$  ( $\pi/2$ ) and the subsequent fine adjustment of one of the phases to maximize the measured correlations.

We found the optimal pumping power to be  $\sigma \approx 0.25$ , corresponding to operation well below the threshold. For these pumping conditions, we measured  $V_{X^-} = -7.1 \pm 0.5$  dB;  $V_{Y^+} = -6.2 \pm 0.5$  dB for the frequency range 50 to 300 kHz (see Fig. 2). Increasing the pump power does not improve the entanglement level due to the enhanced phase noise influence. Further down in the audio frequency band, the entanglement is extremely vulnerable to phase noise. The combination of passive stability and active optoelectronic control allows us to achieve entanglement down to below 10 kHz (Fig. 2). However, even the optimized low-frequency noise limited the EPR correlations to  $V_{X^-} = -5.7 \pm 0.6$  dB;  $V_{Y^+} = -5.2 \pm 0.6$  dB.

We obtain the quadratures of the optical field  $V_Q^o$  characterizing its entanglement by correcting the measured variances  $V_Q$  by the non-unity quantum efficiency of the detectors  $\eta^{\text{det}}$  as

$$V_Q = \eta^{\text{det}}(V_Q^o - 1) + 1, \quad (6)$$

Using the average detector efficiency [15] (see Methods)  $\eta^{\text{det}} = \sqrt{\eta_1^{\text{det}} \eta_2^{\text{det}}} = 0.945$ , we obtain the following variances of the light modes for the data presented in Fig. 2:  $V_{X^-}^o = -8.3 \pm 0.6$  dB;  $V_{Y^+}^o = -7.1 \pm 0.5$  dB and  $V_{X^+}^o = 10.0 \pm 0.5$  dB;  $V_{Y^-}^o = 9.3 \pm 0.6$  dB. From that we obtain the entanglement measures for the optical fields:  $\mathcal{E}_c^2 = 0.029 \pm 0.007 \ll 1$  and  $V^{\text{EPR},c} = 0.34 \pm 0.04 \ll 2$  ( $-7.7 \pm 0.5$  dB below the entanglement boundary). To the best of our knowledge, this is the highest level of EPR entanglement achieved between beams at disparate wavelengths.

To fully characterize our EPR state, we focus on its pu-

urity, which is directly related to the twin-photon nature of the parametric down-conversion process. For a Gaussian state with the covariance matrix  $\mathbb{V}$  the state purity is given by  $\mu = 1/\sqrt{\text{Det}\mathbb{V}} = 1/\sqrt{V_{X^-}^o V_{Y^-}^o V_{X^+}^o V_{Y^+}^o}$  [28] which yields  $\mu = 0.63 \pm 0.16$ . Our results compare favorably with the highest to date two-colour entanglement with  $V^{\text{EPR},c} = 0.38$  and with purity 0.11 (corrected by the reported  $\eta^{\text{det}}$ ) observed in the MHz range [18]. High purity is especially relevant for quantum enhancement of interferometry where both quadratures can contain useful information [29, 30].

We have presented experimental realization of the EPR entangled state of light between modes of different colours with unprecedented degree of entanglement and purity and have expanded the entanglement into the acoustic frequency range.

The present limitations to the observed entanglement are primarily due to the imperfect phase-locking affected by spurious non-linear mixing. Improvement of phase control would make possible to observe even higher levels of entanglement, preserving the state purity. Changing the phase control scheme to a coherent phase-lock [31] and locking the cavity by frequency-shifted modes would eliminate classical noise injection, making it possible to observe two-colour entanglement down to the Hz domain.

The present choice of wavelengths of 1064 nm and 852 nm is motivated by the current laser choice of LIGO and is geared towards the broadband quantum noise reduction in gravitational wave detectors using an ensemble of Caesium atoms [7, 8]. Our approach is readily applicable to entanglement generation between other colours, for example, between 852 nm compatible with the atomic quantum memory and a telecom wavelength.

- \* These authors contributed equally to this work
- [1] Nielsen, M. A. & Chuang, I. L. *Quantum Computation and Quantum Information: 10th Anniversary Edition* (Cambridge University Press, 2010). URL <http://10.1017/CB09780511976667>.
  - [2] Giovannetti, V., Lloyd, S. & Maccone, L. Advances in quantum metrology. *Nature Photonics* **5**, 222–229 (2011). URL <https://doi.org/10.1038/nphoton.2011.35>.
  - [3] Kimble, H. J. The quantum internet. *Nature* **453**, 1023–1030 (2008). URL <https://doi.org/10.1038/nature07127>.
  - [4] Pirandola, S., Eisert, J., Weedbrook, C., Furusawa, A. & Braunstein, S. L. Advances in quantum teleportation. *Nature Photonics* **9**, 641–652. URL <https://www.nature.com/articles/nphoton.2015.154>.
  - [5] Lawrie, B. J., Lett, P. D., Marino, A. M. & Pooser, R. C. Quantum sensing with squeezed light. *ACS Photonics* **6**, 1307–1318 (2019). URL <https://doi.org/10.1021/acsp Photonics.9b00250>.
  - [6] Degen, C. L., Reinhard, F. & Cappellaro, P. Quantum sensing. *Rev. Mod. Phys.* **89**, 035002 (2017). URL <https://link.aps.org/doi/10.1103/RevModPhys.89.035002>.
  - [7] Khalili, F. Y. & Polzik, E. S. Overcoming the standard quantum limit in gravitational wave detectors using spin systems with a negative effective mass. *Phys. Rev. Lett.* **121**, 031101 (2018). URL <https://link.aps.org/doi/10.1103/PhysRevLett.121.031101>.
  - [8] Zeuthen, E., Polzik, E. S. & Khalili, F. Y. Gravitational wave detection beyond the standard quantum limit using a negative-mass spin system and virtual rigidity. *Phys. Rev. D* **100**, 062004 (2019). URL <https://link.aps.org/doi/10.1103/PhysRevD.100.062004>.
  - [9] Duan, L. M., Lukin, M. D., Cirac, J. I. & Zoller, P. Long-distance quantum communication with atomic ensembles and linear optics. *Nature* **414**, 413–418. URL <https://www.nature.com/articles/35106500>.
  - [10] Hammerer, K., Sørensen, A. S. & Polzik, E. S. Quantum interface between light and atomic ensembles. *Rev. Mod. Phys.* **82**, 1041–1093 (2010). URL <https://link.aps.org/doi/10.1103/RevModPhys.82.1041>.
  - [11] Eberle, T., Händchen, V. & Schnabel, R. Stable control of 10 dB two-mode squeezed vacuum states of light. *Opt. Express* **21**, 11546–11553 (2013). URL <http://www.opticsexpress.org/abstract.cfm?URI=oe-21-9-11546>.
  - [12] Steinlechner, S., Bauchowitz, J., Eberle, T. & Schnabel, R. Strong Einstein-Podolsky-Rosen steering with unconditional entangled states. *Phys. Rev. A* **87**, 022104 (2013). URL <https://link.aps.org/doi/10.1103/PhysRevA.87.022104>.
  - [13] Grosse, N. B. *et al.* Observation of entanglement between two light beams spanning an octave in optical frequency. *Phys. Rev. Lett.* **100**, 243601 (2008). URL <https://link.aps.org/doi/10.1103/PhysRevLett.100.243601>.
  - [14] Ou, Z. Y., Pereira, S. F., Kimble, H. J. & Peng, K. C. Realization of the Einstein-Podolsky-Rosen paradox for continuous variables. *Phys. Rev. Lett.* **68**, 3663–3666 (1992). URL <https://link.aps.org/doi/10.1103/PhysRevLett.68.3663>.
  - [15] Schori, C., Sørensen, J. L. & Polzik, E. S. Narrow-band frequency tunable light source of continuous quadrature entanglement. *Phys. Rev. A* **66**, 033802 (2002). URL <https://link.aps.org/doi/10.1103/PhysRevA.66.033802>.
  - [16] Villar, A. S., Cruz, L. S., Cassemiro, K. N., Martinelli, M. & Nussenzveig, P. Generation of bright two-color continuous variable entanglement. *Phys. Rev. Lett.* **95**, 243603 (2005). URL <https://link.aps.org/doi/10.1103/PhysRevLett.95.243603>.
  - [17] Guo, X., Zhao, J. & Li, Y. Robust generation of bright two-color entangled optical beams from a phase-insensitive optical parametric amplifier. *Applied Physics Letters* **100**, 091112 (2012). URL <https://doi.org/10.1063/1.3690876>. <https://doi.org/10.1063/1.3690876>.
  - [18] Wang, N., Du, S. & Li, Y. Compact 6 dB two-color continuous variable entangled source based on a single ring optical resonator. *Applied Sciences* **8**, 330 (2018). URL <https://www.mdpi.com/2076-3417/8/3/330>.
  - [19] Einstein, A., Podolsky, B. & Rosen, N. Can quantum-mechanical description of physical reality be considered complete? *Phys. Rev.* **47**, 777–780 (1935). URL <https://link.aps.org/doi/10.1103/PhysRev.47.777>.
  - [20] Reid, M. D. *et al.* Colloquium: The einstein-podolsky-rosen paradox: From concepts to applications. *Rev. Mod. Phys.* **81**, 1727–1751 (2009). URL <https://link.aps.org/doi/10.1103/RevModPhys.81.1727>.
  - [21] Reid, M. D. Demonstration of the Einstein-Podolsky-Rosen paradox using nondegenerate parametric amplification. *Phys. Rev. A* **40**, 913–923 (1989). URL <https://link.aps.org/doi/10.1103/PhysRevA.40.913>.
  - [22] Cavalcanti, E. G., Jones, S. J., Wiseman, H. M. & Reid, M. D. Experimental criteria for steering and the Einstein-Podolsky-Rosen paradox. *Phys. Rev. A* **80**, 032112 (2009). URL <https://link.aps.org/doi/10.1103/PhysRevA.80.032112>.
  - [23] Simon, R. Peres-Horodecki separability criterion for continuous variable systems. *Phys. Rev. Lett.* **84**, 2726–2729 (2000). URL <https://link.aps.org/doi/10.1103/PhysRevLett.84.2726>.
  - [24] Duan, L.-M., Giedke, G., Cirac, J. I. & Zoller, P. Inseparability criterion for continuous variable systems. *Phys. Rev. Lett.* **84**, 2722–2725 (2000). URL <https://link.aps.org/doi/10.1103/PhysRevLett.84.2722>.
  - [25] Wolf, M. M., Giedke, G., Krüger, O., Werner, R. F. & Cirac, J. I. Gaussian entanglement of formation. *Phys. Rev. A* **69**, 052320 (2004). URL <https://link.aps.org/doi/10.1103/PhysRevA.69.052320>.
  - [26] Drummond, P. D. & Reid, M. D. Correlations in non-degenerate parametric oscillation. II. below threshold results. *Phys. Rev. A* **41**, 3930–3949 (1990). URL <https://link.aps.org/doi/10.1103/PhysRevA.41.3930>.
  - [27] Oelker, E. *et al.* Ultra-low phase noise squeezed vacuum source for gravitational wave detectors. *Optica* **3**, 682–685 (2016). URL <http://www.osapublishing.org/optica/abstract.cfm?URI=optica-3-7-682>.
  - [28] Adesso, G., Ragy, S. & Lee, A. R. Continuous variable quantum information: Gaussian states and beyond. *Open Systems & Information Dynamics* **21**, 1440001 (2014). URL <https://doi.org/10.1142/S1230161214400010>.
  - [29] Yu, H. *et al.* Quantum correlations between light and the kilogram-mass mirrors of ligo. *Nature* **583**, 43–47 (2020). URL <https://doi.org/10.1038/s41586-020-2420-8>.
  - [30] Steinlechner, S. *et al.* Quantum-dense metrology. *Nature Photonics* **7**, 626–630 (2013). URL <https://doi.org/10.1038/nphoton.2013.150>.

- [31] Vahlbruch, H. *et al.* Coherent control of vacuum squeezing in the gravitational-wave detection band. *Phys. Rev. Lett.* **97**, 011101 (2006). URL <https://link.aps.org/doi/10.1103/PhysRevLett.97.011101>.
- [32] Mabuchi, H., Polzik, E. S. & Kimble, H. J. Blue-light-induced infrared absorption in  $\text{KNbO}_3$ . *J. Opt. Soc. Am. B* **11**, 2023–2029 (1994). URL <http://josab.osa.org/abstract.cfm?URI=josab-11-10-2023>.
- [33] Neuhaus, L. e. a. Pyrpl (python red pitaya lockbox) — an open-source software package for fpga-controlled quantum optics experiments. In *2017 Conference on Lasers and Electro-Optics Europe European Quantum Electronics Conference (CLEO/Europe-EQEC)*, 1–1 (2017). URL <https://ieeexplore.ieee.org/document/8087380>.

## METHODS

### NOPO design

The NOPO cavity is designed and tuned to be resonant for both signal (852 nm) and idler (1064 nm) beams while the pump beam (473 nm) is used in a single-pass regime. The cavity has a bow-tie configuration to reduce the negative influence of back-scattered light and to improve the escape efficiency [14]. Quantum light emerges through the output coupling mirror with the transmission coefficient  $T = 12\%$  for both 852 nm and 1064 nm modes. Thus, the cavity bandwidth, free spectral range, and finesse are very similar for both wavelengths. The main NOPO parameters are given in Table I. To minimize astigmatism and contamination from high-order transverse modes, we fine-tune the cavity size and angles of incidence on the mirrors. The NOPO is built in a monolithic aluminum box for better mechanical stability. We use a type-0 periodically poled KTP (PPKTP) crystal (Raicol Crystals Ltd) as the nonlinear medium with an antireflection (AR) coating for 473 nm, 852 nm and, 1064 nm. The desired phase matching is achieved by setting the crystal temperature to  $\approx 63$  °C and stabilizing it to  $\pm 1$  mK. The passive intracavity losses  $\mathcal{L}_j$  are dominated by the PPKTP bulk losses, Table I.

Table I. NOPO main parameters.

Parameter	Value
Intracavity loss for 1064 nm	$0.15 \pm 0.02\%$
Intracavity loss for 852 nm	$0.21 \pm 0.02\%$
Cavity Length	390 mm
Mirror radius of curvature	-38 mm
Free spectral range	769 MHz
Bandwidth	15 MHz
Finesse	52
Threshold power (473 nm)	$320 \pm 16$ mW
PPKTP dimensions	$1 \times 1 \times 10$ mm <sup>3</sup>

### Estimated efficiencies

The measured efficiencies in our system are shown in Table II. The single beam escape efficiency is given by  $\eta_j^{\text{esc}} = T/(T + \mathcal{L}_j)$ , and is the most significant parameter to guarantee high-purity state generation. This leads to an overall escape efficiency  $\eta^{\text{esc}} = \sqrt{\eta_1^{\text{esc}}\eta_2^{\text{esc}}} = 98.5 \pm 0.2\%$  [15]. We also studied the effect of the blue-light-induced infrared absorption (BLIIRA) [32] on the overall escape efficiency and found it negligible under the normal pumping conditions. The combination of ultra-low intracavity losses and BLIIRA-free operation are unprecedented for a two-colour system giving an escape ef-

iciency comparable to the state-of-art degenerate OPO [11].

Table II presents the propagation efficiency  $\eta_j^{\text{pro}}$  from the NOPO output to the detectors, the homodyne efficiency  $\eta^{\text{mm}}$  of the signal-LO mode-matching, and the photodiodes' quantum efficiency  $\eta_j^{\text{det}}$  (see Supplementary Information).

Table II. Estimated efficiencies.

$\lambda$ (nm)	$\eta^{\text{esc}}$	$\eta^{\text{pro}}$	$\eta^{\text{mm}}$	$\eta^{\text{det}}$
1064	$98.7 \pm 0.1\%$	$99.1 \pm 0.3\%$	$98.9 \pm 1.1\%$	$93 \pm 2\%$
852	$98.3 \pm 0.1\%$	$99.0 \pm 0.3\%$	$98.4 \pm 1.5\%$	$96 \pm 2\%$

## ACKNOWLEDGMENTS

We gratefully acknowledge conversations with J. H. Müller and J. Appel. This project has been funded by the InnoFond Denmark through the Eureka Turbo program, by the European Research Council Advanced grant QUANTUM-N, and by the Villum Foundation. T. B. B. was partially supported by CAPES and CNPQ.

## AUTHOR CONTRIBUTIONS

E. S. P. conceived and led the project. T.B.B. and V.N. designed and built the experiment with the help of H.K. and M.L. T.B.B. and V.N. obtained the main experimental results. The paper was written by E. S. P., T.B.B. and V.N., with contributions from H.K. and M.L. E. S. P. and M.L. supervised the research.

## AUTHOR INFORMATION

The authors declare no competing financial interests. Correspondence and requests for materials should be addressed to T.B.B. (tulio.brasil@nbi.ku.dk) or E.S.P. (polzik@nbi.ku.dk).

## DATA AVAILABILITY STATEMENT

The data that support the findings of this study are available from the corresponding author upon reasonable request.



## Pump light

At optimum conditions, the single-pass SFG conversion efficiency is  $\approx 5.5\%/W^2$ , producing more than 900 mW of blue light when the full lasers' power is sent to the nonlinear crystal. In most cases, we run the SFG module at powers between 25% and 70% of the NOPO oscillation threshold (80 - 220 mW) to reduce the overall power fluctuations due to temperature and input power drifts. We found that the long-term power fluctuations were  $< 1\%$ . No intensity stabilization was applied to reduce this effect. Pump power drifts are responsible for parametric gain modulations that can degrade the generated entanglement at low frequencies.

## Parametric gain and oscillation threshold

We inject an intense seed at 1064 nm ( $\approx 100$  mW) in the optical cavity via an HR mirror to check the nonlinear gain. We use this intense injected beam only to calibrate the oscillation threshold and generate coherent amplified (signal and idler) outputs to align and mode-match the local oscillators for homodyne detection.

## LOs and homodyne detectors

The coherent local oscillators are generated by filtering the laser light with mode-cleaning cavities (MCC). The cavities consist of two plane mirrors and a curved mirror in a triangular configuration, with the bandwidth  $\approx 1$  MHz. Built in monolithic aluminum blocks, they perform spatial mode filtering and eliminate beam pointing jitter. In each homodyne detector, we overlap the modes with the corresponding LOs on a 50/50 beam splitter with the visibility  $\mathcal{V}_j$ . The non-unitary visibilities are converted into an effective mode-matching efficiency  $\eta_j^{\text{mm}} = \mathcal{V}_j^2$ . The beam splitter outputs are sent to PIN photodiodes, InGaAs-based (Fermionics, FD500N-1064) for 1064 nm, and silicon-based (Hamamatsu, S5971) for 852 nm. The estimated quantum efficiencies  $\eta_1^{\text{det}}$  and  $\eta_2^{\text{det}}$  are shown in Table II. We calibrate the shot-noise level by blocking the output paths of the NOPO. The detectors provide more than 18 dB shot-noise clearance above the electronic noise with LO powers  $\approx 500 \mu W$ .

All photodiodes are used without protection windows to reduce optical losses. Since the PIN photodiodes are based on different semiconductors, their capacitance is different, inducing a phase delay between the photocurrents. We compensate the photodiodes capacitance mismatch by carefully designing the transimpedance amplifier to improve the broadband correlation measurements.

The local oscillators' optical powers are adjusted to match the shot-noise levels of the two homodyne detectors. To reduce leakage of classical noise from the local oscillators, we optimize the balanced detectors' Common Mode Rejection Ratio (CMRR). We operate the homodyne detectors with  $\text{CMRR}_{1064} = \text{CMRR}_{852} \approx 40$  dB for frequencies below 500 kHz.

## Homodyne angle control

The method used to guarantee double resonance of the NOPO cavity creates spurious back-reflected fields  $c_j$  that are amplified by the parametric gain and follow the same path to the homodyne detection as the entanglement. This field interferes with the local oscillators  $\beta_{\text{LO},j}$  making it possible to probe the phase of the entangled beams and select which quadrature to measure.

The DC signal from the homodyne detectors gives  $E_{\text{dc},j} \propto \beta_{\text{LO},j} c_j \cos \theta_j$ . However, the amplitude  $c_j$  should be maintained as low as possible to reduce classical noise contamination. To measure in the audio band, we use lock beam powers 1 mW for 1064 nm and 30  $\mu W$  for 852 nm. The homodyne photocurrent is amplified with a low-noise amplifier with  $\approx 30$  dB gain and  $\approx 1$  MHz bandwidth, generating an error signal that can be used to lock the phases at  $\theta_j = 0$ . To create an error signal to lock at  $\theta_j = \pi/2$ , we introduce a phase modulation at 800 kHz in the injected 1064 nm lock beam and 600 kHz in the 852 nm local oscillator (see SI1). The homodyne signal is sent to lock-in amplifiers and demodulated giving  $E_{\text{dm},j} \propto \beta_{\text{LO},j} c_j \sin \theta_j$ .  $E_{\text{dc},j}$  and  $E_{\text{dm},j}$  are sent to a feedback controller that generates a signal applied to the LO piezos.



### Data acquisition and processing

We acquire the photocurrents using a low-noise 16 bits analog-to-digital converter (ADC) (Spectrum M2p5913-x4) at a sampling rate of 5 MHz. After digital conversion, the quadratures are combined with relative weights for correlation analysis. Figure 2 was generated by averaging 1000 spectra measurements. Each spectrum is produced with a FFT done over 16000 samples.